**Wind and Structures**, *Vol. 33, No. 4 (2021) 289-304*
https://doi.org/10.12989/was.2021.33.4.289


# Numerical simulation on the typhoon-induced dynamic behavior of transmission tower-line system

Yunzhu Cai*[1], Jiawei Wan**[2], Qiang Xie[3] and Songtao Xue[3]

[1]*College of Civil Engineering, Nanjing Tech University, NO. 30 South Puzhu Road, Jiangbei New District, Nanjing, Jiangsu Province, China, 211816*
[2]*State Environmental Protection Key Laboratory of Atmospheric Physical Modeling and Pollution Control, State Power Environmental Protection Research Institute, No. 10 Pudong Road, Pukou District, Nanjing, Jiangsu Province, China, 210031*
[3]*College of Civil Engineering, Tongji University, No. 1239 Siping Road, Yangpu District, Shanghai, China, 200092*

(*Received January 17, 2021, Revised August 18, 2021, Accepted August 18, 2021*)

**Abstract.** The spatiotemporal impact of typhoons moving across transmission networks is increasingly evident, which may result in the failure of the overhead transmission tower-line (TL) system. The structural design and safety assessment to transmission TL systems that subjected to extreme winds are necessary. This paper aims to provide fundamental insights on the wind field caused by typhoons as well as the typhoon-induced dynamic loads and responses of the transmission TL system, by means of the numerical simulation. This paper offers a numerical scheme to simulate the typhoon-induced wind field on a TL system, in which the movement of the typhoon center and the nonstationary fluctuation of the wind are concerned. In the scheme, the near-surface mean wind speed is calculated based on the radial profile and translation of storms; the nonstationary fluctuation component is generated by a time-varying modulation function. By applying the simulated wind field to the finite element model of TL system, we yield the dynamic responses of the TL system as well as the dynamic loads resulting from the interaction between the structure and wind. Utilizing the evolutionary power spectral density (EPSD) function, the fluctuating wind loads and structural responses are addressed both in the time and frequency domains. Further discussion is done on the typhoon-induced loads by constructing the dynamic equivalent factors. The time-varying equivalent factors show the stationary process, which demonstrates the fading out of the non-stationarity for simulated wind loads. The comparison result indicates that the gust response factor of tower recommended by design codes may not be safe enough when the typhoon impact is concerned.

**Keywords:** dynamic response; transmission tower-line system; typhoon; wind field; wind load

## 1. Introduction

Typhoon/hurricane impacts to the overhead electric transmission tower-line system are widely concerned due to the increasing of typhoon/hurricane events worldwide (IPCC 2013) and the resulting damages and faults to transmission line/networks (Vaiman and Bell 2012). In the southeastern costal region of China typhoon lands frequently each year and leads to failures of the overhead transmission line/networks (Xiao and Duan 2011, Cai and Xie 2019, Cai and Wan 2021). Among all of the failure cases, damages to transmission towers are most adverse, due to less mitigation strategies and time-consuming restoration. Therefore, transmission towers, as the support of transmission line, are fundamental to assure the function and safety of TL systems that are subjected to extreme winds.

Studies on tropical cyclone and typhoon wind field have long drawn extensive attention, most of which employ field measurements, analytical methods and computational simulations as the fundamental approaches (Li and Kareem 2015, Huang and Zheng 2015, Chen and Duan 2018).

Many efforts have been made to generate the near-surface wind field caused by typhoons/hurricanes, in which two main approaches are included. One is combining the finite-difference scheme with nested rectangular grids and then to solve the typhoon-induced steady-state wind field in the planetary boundary layer (Meng and Matsui 1997). Another alternative approach is to develop the parametric wind model with the assumption that the near-surface wind, as a vector, is the combination of the component that related to the storm vortex and the component that related to the storm movement (Lin and Chavas 2012). It is noteworthy the time-varying near-surface wind just accounts for the mean wind and the wind turbulence is not considered. In typhoon events, the wind fluctuation is commonly characterized by the non-stationarity. Hence, evolutionary power spectral density (EPSD) functions, that can uncover the energy distribution over the time and frequency domains simultaneously, are helpful to trace the non-stationary feature of typhoon wind fluctuations. Non-stationary wind fluctuations are usually addressed as uniformly modulated processes, due to the observation results indicating that frequency components included in EPSDs evolve very slightly with time (Huang and Zheng 2015). An available stationary process described by the power spectral density (PSD) function is first adopted for the simulation of non-

*Corresponding author, Ph.D.
E-mail: yunzhucai@njtech.edu.cn
**Corresponding author, Ph.D.
E-mail: jiawei.wan@outlook.com



ISSN: 1226-6116 (Print), 1598-6225 (Online)

stationary wind fluctuations and then extended to nonstationary ones depending on the slow-changing feature. Based on the prescribed/generated PSD/EPSD, stationary/non-stationary processes can be further solved in the time domain and some numerical methods have been proposed/developed to do the solution (Kareem 2008, Tao and Wang 2019, Tao and Shi 2020).

A transmission tower-line system is generally comprised of three parts, the transmission tower, the transmission wire (including conductors and ground wires) and the insulator. Slender towers and flexible wires result in the wind sensitivity for TL systems. Wind-induced interaction between the tower and wires (i.e., the coupling effect) is a tricky issue: the wind load acting on wires is transferred to the tower structure and the vibration of wires makes effects on the tower vibration, which may lead to the tower response amplified remarkably; while the constraints at two ends of the span of wires may change with the tower response, which in turn influences the behavior of wires. Many researchers studied the wind effect on the tower and wires using the approaches of field monitoring (Paluch and Cappellari 2007, Takeuchi and Maeda 2010), wind tunnel tests (Liang and Zou 2015, Xie and Cai 2017, Huang and Lou 2012) and analytical-numerical methods (Battista and Rodrigues 2003, Wang and Chen 2017).

Analyses on typhoon-induced loads and responses of TL systems are less, because the field monitoring data that relating typhoons to TL systems are not easy to get/accumulate and it is hard for artificial wind tunnels to generate the typhoon wind field delicately. Therefore, this paper, combining the developed typhoon/hurricane models with the TL system modeling techniques, provides fundamental insights on the numerical simulation of the typhoon impact to TL systems, by which the typhoon-induced dynamic loads and buffeting of TL system are concerned and discussed. In section 2, the typhoon wind simulation is accomplished with the radial model of tropical cyclones, the parameter-based calculation rule of surface mean winds, the vertical profile of surface mean winds and the simulation of non-stationary wind fluctuations included. In section 3, the typhoon wind loading to TL systems is clarified and then dynamic simulations of an example TL system subjected to a practical typhoon event is carried out. In section 4, simulation results related to structural responses and wind loads are yielded and discussed both in time and frequency domains using EPSDs. In section 5, further discussion is done on the typhoon-induced dynamic loads by constructing two static equivalent factors. In the last, some important methods/results that used/obtained in the simulation study are concluded.

## 2. Wind simulation

In terms of the large scale, typhoon shaped as a storm vortex moves over the ocean or ground. As a result, the wind intensity and direction at the position of interest varies with the storm moving and physical parameters of typhoon changing. In terms of the small scale, with the mean wind intensity varying with time, the wind fluctuation is characterized by the non-stationarity. In the following simulation, both of the large-scale and small-scale calculations/simulations are concerned.

### 2.1 Radial profile of typhoon storms

Radial profiles, used to describe the variance of wind speed in a horizontal plane of storm vortex, have been observed, analyzed and modeled by many researchers. For engineering application, an engineer named William Rankine first assumed an experience-based radial profile model, and then the Rankine model was adopted and corrected by Schloemer Eq. (1) (Schloemer 1954).

$$V=\begin{cases} V_m\left(r/r_m\right), & r<r_m \\ V_m\left(r_m/r\right)^x, & r\geq r_m \end{cases} \tag{1}$$

$V$ is the magnitude of wind speed at the radius of $r$; $V_m$ is the maximum wind speed along the radial direction and $r_m$ is the corresponding radius; $x$ is the correction factor, taken to be 1 for an ideal vortex and less than 1 under real situations. Schloemer proposed that the variance of the air pressure along the radial direction can be expressed with a corrected rectangular hyperbola, based on which a specific radial model related to the air pressure was built by Holland Eq. (2) (Holland and Belanger 2011).

$$p(r)=p_0+\Delta p\exp\left[-\left(r_m/r\right)^B\right] \tag{2}$$

$p$ is the pressure at the radius of $r$; $p_0$ is the air pressure at the center of vortex (unit: hPa); $B$ is the correction factor with the variance range of 0.5~2.5; $\Delta p$ is the pressure difference between the atmospheric pressure and $p_0$. According to the air-pressure-based Holland model, the radial profile of wind speed can be generated by relating the wind intensity to the air pressure Eq. (3).

$$V(r)=\left\{\left(\frac{r_m}{r}\right)^B\frac{100B\Delta p\exp\left[-\left(r_m/r\right)^B\right]}{\rho}+\frac{r^2f^2}{4}\right\}^{1/2}-\frac{fr}{2} \tag{3}$$

where

$$B=\frac{e\rho\left(V_m^2+fV_mr_m\right)}{100\Delta p} \tag{4}$$

$\rho$ is the air density; $e$ is the base of logarithm; $f$=2Ωsin$\varphi$ is the Coriolis coefficient with the rotation angular velocity of the earth Ω=7.292*10$^{-5}$rad/s and $\varphi$ is the latitude of the storm center. The power factor 1/2 in Eq. (3) can also be replaced by an empirical parameter that determined by observation results (Holland and Belanger 2011).

Both of the corrected Rankine model and Holland model are a sort of empirical models taking the parameter $x$ or $B$ as the correction factor. The maximum wind speed $V_m$ and its corresponding radius $r_m$ are two significant observation data for figuring out the radial profile. Differing from the above two classical empirical models, Emanuel et. al (Emanuel and Rotunno 2011, Chavas and Lin 2015, Chavas Line 2016) proposed and developed a physical-parameter-based

Table 1 Parameters of typhoon storms (http://www.typhoon.org.cn/)

| Typhoon storm (#) | a | b | c | d |
|---|---|---|---|---|
| Central pressure ($p_0$) | 982 hPa | 970 hPa | 945 hPa | 915 hPa |
| Maximum wind ($V_m$) | 25 m/s | 35 m/s | 48 m/s | 60 m/s |
| Location | 19.0°N, 110.7°E | 25.0N°, 119.4°E | 21.8°N, 114.1°E | 19.9°N, 111.3°E |
| Observation point ($V_b$, $r_b$) | 15.5 m/s, 200 km | 15.5 m/s, 300 km | 15.5 m/s, 280 km | 15.5 m/s, 300km |
| Correction factor ($x$) (Riehl 1954) | 0.5 | | | |
| Radiative-subsidence rate ($w$) (Chavas and Lin 2015) | 2 mm/s | | | |
| Surface drag coefficient ($C_D$) (Donelan and Haus 2004) | $C_D = \begin{cases} 6.16\times10^{-4} & V \le 6m/s \\ 5.91\times10^{-5}V + 2.614\times10^{-4} & 6 \le V \le 35.4m/s \\ 2.4\times10^{-3} & V \ge 35.4m/s \end{cases}$ | | | |
| ratio of exchange coefficents of enthalpy and momentum ($\xi$) (Chavas and Lin 2015) | $\xi = 0.00055V_m^2 - 0.0259V_m + 0.763$ and $\xi \le 1$ | | | |

* The correction factor $B$ is calculated by Eq. 4 with $r_m$ determined by the solution of Emanuel model.

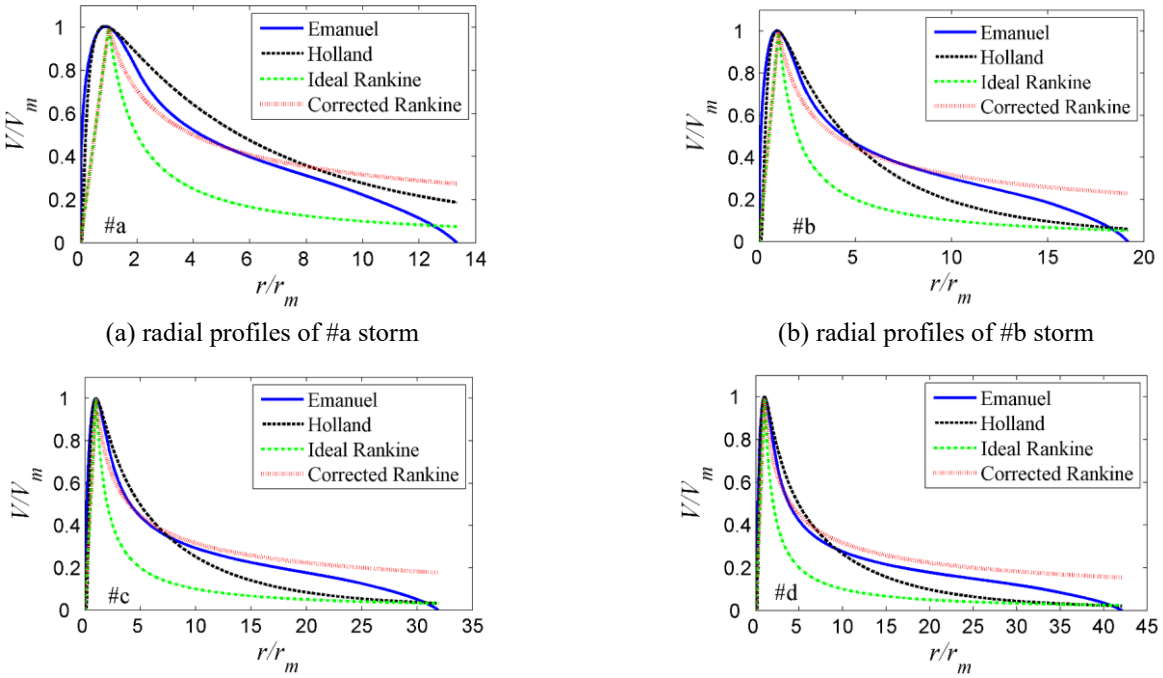


(a) radial profiles of #a storm

(b) radial profiles of #b storm

(c) radial profiles of #c storm

(d) radial profiles of #d storm

Fig. 1 Comparisons of radial profiles

radial model for the storm vortex, in which the storm is finally divided into two regions depending on the kinematic and thermodynamic properties, i.e., the descending outer region Eq. (5) and ascending inner region Eq. (6). The two regions are jointed depending on the continuity of the angular momentum of air masses.

Outer region:

$$\frac{\partial M^{outer}}{\partial r} = \frac{2C_D}{w}\frac{(rV)^2}{r_0^2 - r^2} \tag{5}$$

Inner region:

$$\left(\frac{M^{inner}}{M_m}\right)^{2-\xi} = \frac{2(r/r_m)^2}{2-\xi+\xi(r/r_m)^2} \tag{6}$$

At joint point '$a$':

$$\begin{cases} M_a^{outer} = M_a^{inner} \\ \left(\dfrac{\partial M^{outer}}{\partial r}\right)_{r=r_a} = \left(\dfrac{\partial M^{inner}}{\partial r}\right)_{r=r_a} \end{cases} \tag{7}$$

where $M = rV + \frac{1}{2}fr^2$;

$M$ is the angular momentum of the air mass at the radius of $r$; $C_D$ is the surface drag coefficient; $w$ is the magnitude of the radiative-subsidence rate in the free troposphere; $r_0$ is the radius where the rotational wind is zero; $M_m$ is the angular momentum at the radius of maximum wind; $\xi$=$C_k$/$C_D$ is the ratio of exchange coefficents of enthalpy and momentum; $r_a$ and $V_a$ are the radius and wind speed at the

joint point of two regions. The complete radial profile can be calculated from the outer region to the inner region, during which three environmental parameters (i.e., $C_D$, $w$ and $\xi$) and three storm parameters (i.e., $r_0$, $r_m$ and $V_m$) are involved. It is uneasy to observe and measure the vaules of $r_0$ and $r_m$ directly. Hence, the calculation is generally done by utilizing an observation point located in the outer region (i.e., $V_b$ and $r_b$. $r_b$ is the radius where the wind speed is valued as $V_b$). Then, $r_0$ is yielded by solving Eq. 5 and the outer profile can be figured out with the $C_D$ and $w$ given. The radius of maximum wind $r_m$ as well as the joint point 'a' can be solved by connecting the outer region to the inner region.

Taking four storm vortexes of typhoons as the example, Fig. 1 compares the radial profiles generated by the Rankine, Holland and Emanuel models. The basic information of the four typhoon storms are listed as follows (Table 1). From Fig. 1, we see the Emanuel-based radial profile is always enveloped by the other three empirical radial profiles. In the following simulation, the Emanuel model is adopted to calculate the time-varying mean wind speed, considering its efficient solutions and few empirical parameters involved.

### 2.2 Near-surface mean wind speed

The Emanuel model assumes the storm vortex is symmetric and stationary. In reality, the storm is characterized by non-symmetry due to the translation of storm and the change of external environment. Therefore, the near-surface mean wind speed is determined by the combination of two components Eq. (8): one is related to the storm itself and noted as $\vec{V_r}$; the other is the background component related to the local environment and noted as $\vec{V_t}$.

$$\vec{U} = \alpha_r \vec{V_r} + \alpha_b \vec{V_t} \tag{8}$$

The magnitude of the storm component equals to the wind speed that calculated by the radial profile of storm and that of the background component is taken to be the translation velocity of the storm. $\alpha_r$ and $\alpha_b$ are the reduction factor and participation factor of the storm component and background component, respectively. As to the directions of the two components, the storm component is modified with the in-flow angle $\alpha$ (see Eq. 9) (Phadke and Martino 2003), and the background component is modified with the rotation angle $\beta$ taken to be 20° (anti-clockwise in the northern hemisphere) (Lin and Chavas 2012).

$$\alpha = \begin{cases} 10^{\circ}\left(1+\dfrac{r}{r_m}\right), & 0 \le r < r_m \\ 20^{\circ}+25^{\circ}\left(\dfrac{r}{r_m}-1\right), & r_m \le r < 1.2r_m \\ 25^{\circ}, & r \ge 1.2r_m \end{cases} \tag{9}$$

Then, the near-surface mean wind speed $\boldsymbol{U}$ is figured as

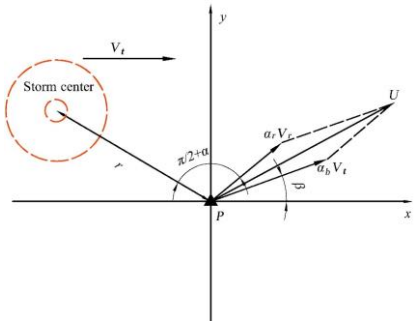


Fig. 2 Near-surface mean wind speed

Fig. 2. $P$ is the position of interest. When the distance $r$ is larger than $r_a$, the outer region model of radial profile is used, otherwise the inner model is used to calculate $V_r$. Considering the wind that 10m over the surface, the reduction factor $\alpha_r$ and participation factor $\alpha_b$ are taken to be 0.85 and 0.55 respectively according to the observation results (Lin and Chavas 2012). It is noteworthy that the rule for the surface drag coefficient $C_D$ changes when the typhoon storm moves from the ocean to the ground. The calculation of $C_D$ shown in Table 1 accounts for the ocean surface, while for the ground surface, $C_D$ is determined by Eq. (10) (Meng and Matsui 1997).

$$C_{Dg} = \frac{\kappa^2}{\left\{\ln\left[\left(h^* + 10 - d\right)/z^*\right]\right\}^2} \tag{10}$$

$\kappa$ is the karman constant taken to be 0.4; $z^*$ is the roughness length determined depending on the terrian type; $h^*$is the mean height of roughness elements on the ground and $h^*=11.4(z^*)^{0.86}$; $d$ is the zero-plane displacement taken to be 0.75 $h^*$.

The near-surface mean wind speed $U$ with the averaging of 10 mins is concerned in the simulation, while measured wind speed data are usually yielded every 2 min or shorter. Therefore, the time-scale conversion is necessary from the measured data to the required near-surface mean wind. The conversion law given by Simiu *et al*. (Simiu and Scanlan 1996) is used Eq. (11).

$$\frac{U_T(z)}{U_{3600}(z)} = \left[1 + \frac{\varepsilon^{0.5} c(T)}{2.5\ln(z/z_0)}\right] \tag{11}$$

$T$ is the time duration; 3600 in the numerator term means $T$ = 3600s. $z$ is the height of concern; $z_0$ is the surface roughness length. $\varepsilon$ is a roughness-length-related empirical coefficient; $c(T)$ is a time-duration-related statistical parameter.

### 2.3 Vertical mean wind speed profile

The vertical profile describes the variance of the wind along the height/altitude. The power law and logarithm law are the two commonest rules used to shape the vertical profile. Field monitoring studies on tropical cyclones indicate that the logarithm law can effectively approximate the wind distribution in the height range of 0~100 m

(Vickery and Wadhera 2009), and therefore it is widely adopted to describe and simulate the typhoon wind field. This paper uses the logarithm law shown in Eq. (11) to calculate the wind speed at different heights.

$$\frac{U(z_i)}{U(z_j)} = \frac{\ln(z_i/z_0)}{\ln(z_j/z_0)} \tag{12}$$

$U(z_i)$ and $U(z_j)$ are the mean wind speed at the height of $z_i$ and $z_j$, respectively. $z_0$ is the surface roughness length. When the positon of interest is over the gound, $z_0$ is equivalent to $z^*$ shown in Eq. (10) and valued based on the terrian type. If the position of interest is over the sea, $z_0=\alpha_0*C_D*[U(10)]^2/g$ (Charnock 1955), in which $\alpha_0$ is a constant varying in the range of 0.015-0.035, $C_D$ is the surface drag coefficient and calculated according to Table 1, $U(10)$ is the mean wind speed at 10m over the sea, g is the gravitational acceleration.

Considering the time history, the near-surface mean wind speed can be further expressed as Eq. (13) by adopting the time function $f(t)$.

$$\bar{U}(z,t) = U(z) \times f(t) \tag{13}$$

$\bar{U}(z,t)$ represents the resultant mean wind speed at the height of $z$ and time of $t$. If we assume $U(z)$ is the maximum mean wind speed at the height of $z$ during the time period of concern, then $f(t)$ should be a function whose value is always no larger than one. The tendency of $f(t)$ is influenced by the movement of typhoon storms.

### *2.4 Nonstationary fluctuation*

The typhoon wind fluctuation shows the non-stationarity with the time-varying mean wind. To simulate the wind fluctuation, we first assume the frequency structure contained in the fluctuation do not change with time and then the evolutionary power spectral density (EPSD) method is used to generate the fluctuation. The wind fluctuation is treated as a uniformly modulated evolutionary stochastic process that written as Eq. (14).

$$u(z,t) = A(z,t) \cdot \bar{u}(z,t) \tag{14}$$

$u(z, t)$ represents the wind fluctuation at the height of z and time of $t$; $A(z, t)$ is the modulation function given by $A(z, t) = I_u U(z, t)$ with $I_u$ being the turbulence intensity and determined by the terrain type; $\bar{u}(z,t)$ represents a stationary Gaussian process with its variance taken to be one. The stationary process $\bar{u}(z,t)$ has the spectral expression shown as Eq. (15).

$$\bar{u}(z,t) = \int_{-\infty}^{\infty} e^{i\omega t} dZ(z,\omega) \tag{15}$$

$\omega$ is the angular frequency and $Z(z, \omega)$ is a zero-mean orthogonal incremental process with the property shown as Eq. (16).

$$E\left\{dZ(z_i,\omega) \times \overline{dZ(z_j,\omega)}\right\} = \tilde{S}(z_i,z_j,\omega)d\omega \tag{16}$$

If $z_i = z_j = z$, $\tilde{S}(z_i, z_j, \omega)$ means auto power spectrum density (PSD) of $\bar{u}(z,t)$; else if $z_i \neq z_j$, $\tilde{S}(z_i, z_j, \omega)$ means the cross-PSD between $\bar{u}(z_i,t)$ and $\bar{u}(z_j,t)$. According to Eqs. (14)-(16), the spectral expression of wind fluctuation $u(z, t)$ can be further written as Eq. (17), and the corresponding EPSD is written as Eq. (18).

$$u(z,t) = \int_{-\infty}^{\infty} A(z,t) e^{i\omega t} dZ(z,\omega) \tag{17}$$

$$S(z_i,z_j,\omega,t) = A(z_i,t)\overline{A(z_j,t)}\tilde{S}(z_i,z_j,\omega) \tag{18}$$

If $z_i = z_j = z$, $S(z_i, z_j, \omega, t)$ means auto-EPSD of $u(z, t)$; else if $z_i \neq z_j$, $S(z_i, z_j, \omega, t)$ means the cross-EPSD between $u(z_i, t)$ and $u(z_j, t)$. From Eq. (18), we see the EPSD of the nonstationary wind fluctuation is expressed with a stationary PSD multiplied by the slowly time-varying modulation function. The stationary cross-PSD $\tilde{S}$ is calculated by Eq. (19).

$$\tilde{S}(z_i,z_j,\omega) = \mathrm{Coh}(z_i,z_j,x_i,x_j,\omega) \cdot \sqrt{\tilde{S}(z_i,\omega)\tilde{S}(z_j,\omega)} \tag{19}$$

where $\tilde{S}(z_i, \omega)$ and $\tilde{S}(z_j, \omega)$ are the auto-PSD at the height of $z_i$ and $z_j$ respectively; $\mathrm{Coh}(z_i, z_j, x_i, x_j, \omega)$ is the coherence function of two arbitrary points in the $z$-$x$ plane and the calculation rule proposed by Davenport is adopted here (Eq. 20).

$$\mathrm{Coh}(z_i,z_j,x_i,x_j,\omega) = \exp\left(-\frac{\omega}{2\pi} \cdot \frac{\sqrt{\lambda_z^2(z_i-z_j)^2 + \lambda_z^2(x_i-x_j)^2}}{0.5\left[U(z_i)+U(z_j)\right]}\right) \tag{20}$$

The above coherence function takes the correlations along the axis $z$ and axis $x$ into account simultaneously. Hence, the PSD $\tilde{S}$ is further written as $\tilde{S}(z_i, z_j, x_i, x_j, \omega)$. The exponential decay coefficient $\lambda z$ and $\lambda x$ in Eq. (20) are taken to be 10 and 16, respectively.

Consequently, the fluctuation model has its EPSD matrix shown as Eq. (21).

$$\mathbf{S}(\omega,t) = \mathbf{A}(t)\tilde{\mathbf{S}}(\omega)\bar{\mathbf{A}}^T(t) \tag{21}$$

where $\mathbf{A}(t) = \left[A(z_1,t), A(z_2,t), \ldots, A(z_n,t)\right]$;

$$\tilde{\mathbf{S}}(\omega) = \begin{bmatrix} \tilde{S}_{11}(\omega) & \tilde{S}_{12}(\omega) & \cdots & \tilde{S}_{1n}(\omega) \\ \tilde{S}_{21}(\omega) & \tilde{S}_{22}(\omega) & \cdots & \tilde{S}_{2n}(\omega) \\ \vdots & \vdots & \ddots & \vdots \\ \tilde{S}_{n1}(\omega) & \tilde{S}_{n2}(\omega) & \cdots & \tilde{S}_{nn}(\omega) \end{bmatrix};$$

$\tilde{S}_{ij}(\omega) = \tilde{S}(z_i, z_j, x_i, x_j, \omega)$; $i, j = 1, 2, \ldots, n$; $n$ is the number of points that concerned in the space; $\bar{\boldsymbol{A}}^T(t)$ is the conjugate transpose of $\boldsymbol{A}(t)$.

The auto-PSD $\tilde{S}_{ii}(z_i, x_i, \omega)$ is described by the Kaimal spectrum here, which is a kind of classical stationary wind fluctuation spectra considering the effects of altitudes.

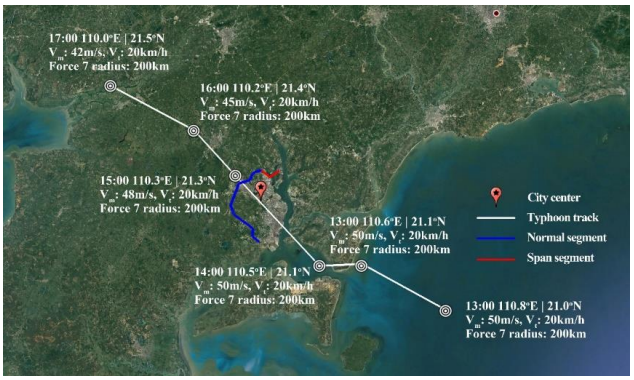


Fig. 3. Typhoon event

* The blue line/normal segment and red line/span segement in Fig. 3 denote two segements of an example transmission line that will be involved in the following study.

Improved by Simiu, the Kaimal spectrum is expressed as Eq. (22) and widely applied to the high-rise and large-span buildings/infrastructures.

$$\frac{\omega \tilde{S}(z,\omega)}{U_*^2} = \frac{200f}{(1+50f)^{5/3}} \tag{22}$$

where $f = \frac{\omega z}{U(z)}$; $U_*^2 = \frac{kU(z)}{\ln(z/z_0)}$;

$f$ is called the similarity-law-based coordinate; $U(z)$ is mean wind speed at the height of $z$; $U_*$ is the called the friction velocity of the flow; $k$ is the Von Karman constant taken to be 0.4; $z_0$ is the ground-surface roughness length. It is noteworthy that the Kaimal-based auto-PSD $\tilde{S}_{ii}(z_i, x_i\omega)$ is just related to the height $z$, that is, the auto-PSDs at the same height are identical.

Based on the prescribed PSD/EPSD, the stationary/nonstationary processes can be solved using mathematical methods, such as the Hilbert trans-form approach, the wavelet-based method and the spectral representation method. Here, the Deodatis simulation (Shinozuka and Deodatis 1991), a modified spectral representation method, is used to simulate the fluctuating wind field. The matrix $\tilde{\mathbf{S}}(\omega)$ in Eq. 21 is a self-conjugate matrix and can be expressed as $\tilde{\mathbf{S}}(\omega) = \mathbf{H}(\omega)\overline{\mathbf{H}}^T(\omega)$ by Cholesky decomposition. $\mathbf{H}(\omega)$, as a lower triangular matrix, has its elements expressed as $\mathrm{H}_{jk}(\omega) = |\mathrm{H}_{jk}(\omega)|\exp[\mathrm{i}\theta_{jk}(\omega)]$, where $j$=1, 2, …, $n$; $k$=1, 2, …, $j$; $j \geq k$; $\theta_{jk}(\omega) = \tan^{-1}\{\mathrm{Im}[\mathrm{H}_{jk}(\omega)]/\mathrm{Re}[\mathrm{H}_{jk}(\omega)]\}$. Assume $t$=$p\Delta t$ and $\omega_{ml}$=($l$-1) $\Delta\omega$ + ($m$/$n$) $\Delta\omega$, where $m$=1, 2, …, $n$; $l$=1, 2, …, $N$; $\Delta\omega$=$\omega_u$/$N$. $\omega_u$ is the upper cutoff frequency beyond which $\tilde{\mathbf{S}}(\omega)$ is taken to be a zero matrix. When $\Delta\omega$ is small enough (i.e., $N$ goes to infinity), the stationary process $\bar{u}(z,t)$ can be simulated by Eq. (23).

$$\bar{u}(z_j, p\Delta t) = \mathrm{Re}\left\{\sum_{m=1}^{j} g_{jm}^{(\mathrm{i})}(q\Delta t)\exp[\mathrm{i}(m\Delta\omega/n)(p\Delta t)]\right\} \tag{23}$$

where $p$ = 0, 1, …, $n$×$M$-1; $q$ is the remiander of $p$/ $M$; $M$ = 2$N$; and

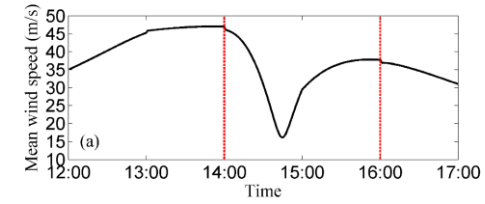


(a) magnitude

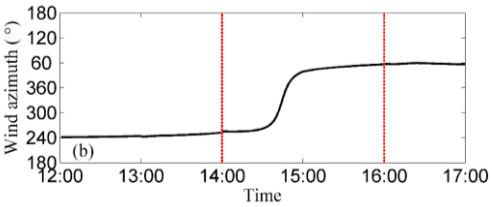


(b) direction (the azimuth that clockwise from the north)

Fig. 4.Time history of the mean wind speed in the city region

$$g_{jm}^{(\mathrm{i})}(q\Delta t) = \sum_{l=0}^{M-1} B_{jm}(l\Delta\omega)\exp\left[\mathrm{i}(l\Delta\omega)(q\Delta t)\right] \tag{24}$$

$$B_{jm}(l\Delta\omega) = 2\left|H_{jm}\left(l\Delta\omega + m\Delta\omega/n\right)\right| \cdot \sqrt{\Delta\omega} \cdot \exp\left[-\mathrm{i}\theta_{jm}\left(l\Delta\omega + m\Delta\omega/n\right)\right] \cdot \exp\left(\mathrm{i}\tilde{S}_{ml}^{(\mathrm{i})}\right) \tag{25}$$

Eqs. (24) and (25) indicate $B_{jm}(l\Delta\omega)$ and $g_{jm}(q\Delta t)$ are a fast Fourier transform (FFT) pair for the given $j$ and $m$. Hence, Eq. (23) can be easily solved using the FFT technique. Then, the wind fluctuation shown as Eq. (14) is calculated and the corresponding EPSD is achieved according to Eq. (21).

### 2.5 Example

Taking a practical typhoon event as the example (Fig. 3), the time-varying nonstationary wind field is simulated using the methods explained above. Concerning the region of city center (near 110.37°E |21.26°N) shown in Fig. 3, six continuous time slices are involved.

The typhoon data shown in Fig. 3 is measured at 10 m over the surface and with the time averaging of 2 min (http://www.typhoon.org.cn/).The force 7 radius means the storm radius where the wind intensity reaches grade 7 on the Beaufort scale in the outer region of the storm. Here, we assume the wind speed at the force 7 radius equals to 15.5m/s (i.e., $V_b$=15.5m/s and $r_b$=force 7 radius for calculating the radial profile model described by Eqs. (5)-(7)). For Eq. (11), we have the time-duration-related statistical parameter $c$=0.956 with $T$=2 min and $c$=0.36 with $T$=10min. Considering the terrain type of the target region, the surface roughness length $z^*$ in Eq. (11) and $z_0$ in Eqs. (12)-(13) are taken to be 0.02. Then, Combining the Emanuel radial model with the near-surface mean wind speed model, the time history of the wind speed at 10 m

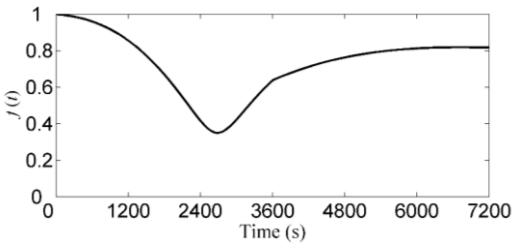


Fig. 5 The time profile of the mean wind speed in the city region

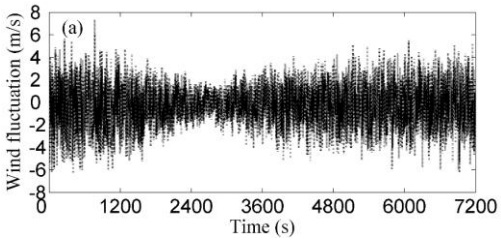


(a) time history

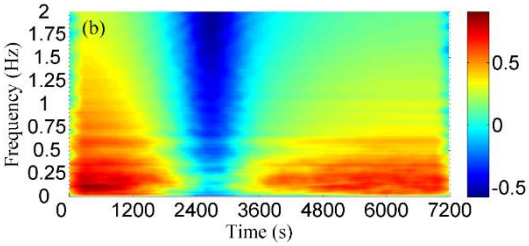


(b) EPSD

Fig. 6 Nonstationary fluctuation of the wind at 10 m over the ground

over the ground with the time averaging of 10 min is generated for the city center (see Fig. 4).

According to Figs. 3 and 4, we have the typhoon storm moves to the inland sea at 14:00 which leads to the maximum mean wind speed for the city of concern and then the storm crosses the city region during 14:00 ~ 16:00 which leads to significant changes of the wind intensity and azimuth. In the following, we take the time period of 14:00~16:00 (7200 seconds in total) into consideration. Then, Fig. 5 shows the time profile of the mean wind speed that normalized by the maximum value.

The wind fluctuation is simulated using the above EPSD-based nonstationary model with the turbulence intensity at 10m over the ground (i.e., $I_u$) valued as 0.14. Fig. 6 shows the simulation results of the wind fluctucation in terms of the time history and EPSD. From the EPSD (Fig. 6(b)), we see the frequency range of 0~0.25Hz accounts for the dominate role in the time history, and the fluctuation intensifies/weakens along with the growing/decreasing of the mean wind speed.

Considering the time period of 14:00 ~ 16:00, Fig. 7 further gives the typhoon-induced total wind speed (10 m over the ground) at the city center (110.37°E |21.26°N), which is calculated by the sum of the mean wind speed that shown in Fig. 4(a) and the wind fluctuation that shown in Fig. 6(a), with the change of the wind azimuth given by Fig. 4(b).

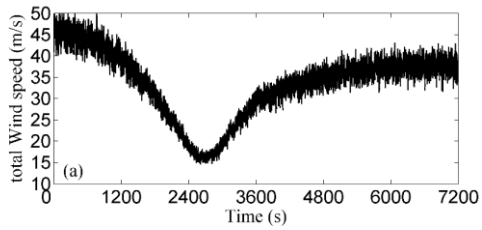


(a) total wind speed

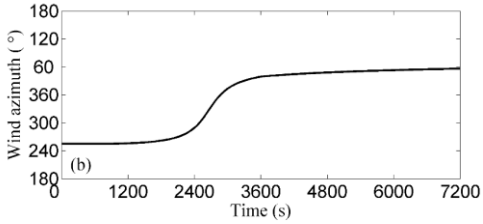


(b) wind azimuth

Fig. 7 Nonstationary typhoon wind

## 3. Wind loading to a tower-line system

### *3.1 Wind field to TL system*

The typhoon wind may not impact the TL system in a perfect transverse direction, due to the geo-spatial distribution of TL system and time-varying movement of the typhoon storm. To consider the skew wind conditions, a Cartesian coordinate system (*x*-*y*-*z* shown in Fig. 8) is first settled with the along-line (longitudinal) direction being the *x* axis, the cross-line (transverse) direction being the *y* axis and the vertical direction being the *z* axis. The typhoon wind to a TL system generally consists of three components under the three-dimensional space, i.e., the yaw wind which is decomposed into the time-varying mean wind $U$ and along-wind fluctuation $u$, the lateral wind fluctuation $v$ and the vertical wind fluctuation $w$. Three components of the wind turbulence $u$, $v$ and $w$ can be approximated by nonstationary evolutionary processes. In this study, given the limited effect of $v$ and $w$ on the TL system, we take the two turbulence components to be zero. According to Fig. 8, the direction of the yaw wind is described by the wind azimuth $\psi$ whose magnitude is defined as clockwise from the north; the along-line direction is described by the clockwise azimuth $\theta$; the yaw angle of wind is defined as the angle $\varphi$ down from the positive axis $x$; then the wind angle of attack to the TL system is calculated by (90°-$\varphi$).

Typhoon wind at any point of concern in the TL system can be generated using the wind simulation methods illustrated in the previous sections. In the following simulation, we take the two-span TL system shown in Fig. 8 as the example. The joints between the insulator and the conductor at two end towers are fixed along the line direction. Considering the scale of typhoon storm is much larger than the span of line, the multi-span effect induced by the typhoon wind is neglected. Then the two-span TL system is reasonable when we just take the center tower as the study object, as the influence of non-adjacent conductors on the tower structure under winds has been proved to be slight by simulations. This example TL system

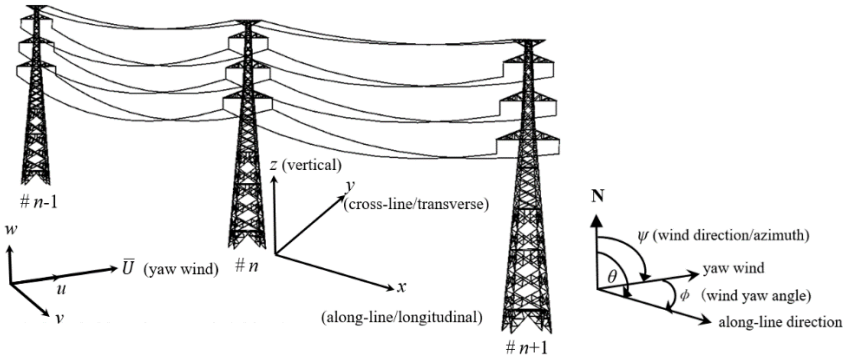


Fig. 8 Wind to the TL system

Table 2 Design information of the example two-span TL system

| | |
|---|---|
| Suspension tower structures | |
| Type | Double-circuit angle-steel tower |
| Total height (m) | 45.5 |
| Steel type | Q345, Q235 |
| Leg distance (m) | 6.4 |
| Natural vibration frequency (Hz) | 2.037 (transverse), 2.047 (longitudinal) |
| Transmission wires (including conductors and ground wires) | |
| Type | LGJQ-300/40 (two-bundled conductors), LGJQ-95/55 (ground wires) |
| Line density (kg/m) | 2.2660 (conductors), 0.7077 (ground wires) |
| Outer diameter (mm) | 47.88 (conductors), 16 (ground wires) |
| Line information | |
| Span (m) | 300 (left), 243 (right) |
| Direction (azimuth) | 126.29° (clockwise from the north) |
| Terrain type | Open (type B in the Chinese code) |

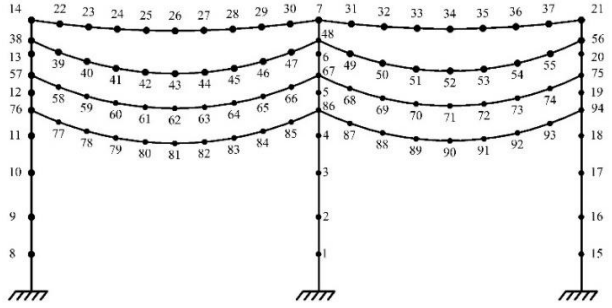

(a) spatial points

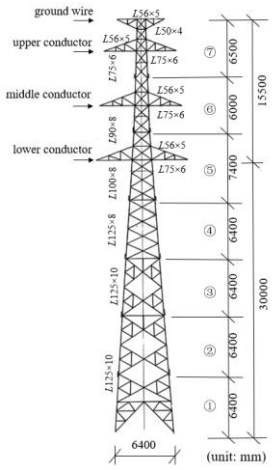


(b) the suspension tower

Fig. 9 TL system

is a part of the practical transmission line shown in Fig. 3, with its along-line direction $\theta$=126.29° and two spans $L_1$=300 m, $L_2$=243 m. More design information of the example tower-line system is listed in Table 2.

Considering the typhoon event simulated in section 2.5, time histories of the wind speed at spatial points of example TL system (see Fig. 9(a)) can be generated. As the support structure, suspension transmission towers, shown as Fig. 9(b), is divided into seven sections along its height and with four cross arms connected.

Jointly considering the time-varying wind azimuth $\psi$ and the constant line azimuth $\theta$, we calculate the wind yaw angle $\varphi$ and get its time history shown as Fig. 10. With the typhoon storm crossing the city center (Fig. 3), the wind yaw angle changes remarkably during the time of 2400s ~ 3600s shown as Fig. 10.

### *3.2 Wind load on TL system*

According to the quasi-steady theory, the wind load

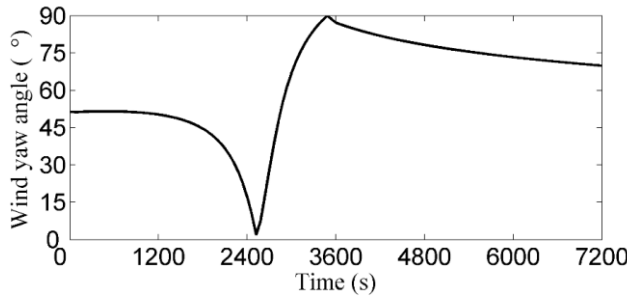


Fig. 10 Time history of wind yaw angle

acting on a structure is calculated by Eq. (26)

$$F_w = \frac{1}{2}\rho_{air}\left(\bar{U}+u-\dot{X}\right)^2 \cdot C_D A_s \tag{26}$$

where $\rho_{air}$ is the air density taken to be 1.25kg/m$^3$; $\bar{U}$ is the mean wind speed and $u$ is the wind fluctuation at geo-spatial points; $\dot{X}$ represents the along-wind velocity response of the structure; $C_D$ is the drag coefficient that jointly determined by the size, shape and shielding rate of the structure/structural components; $A_s$ is the wind-loading area that generally equivalent to the projection area of the structure along the wind direction. From Eq. (260, the wind load is related not only to the wind speed but also to the structural velocity, which leads to the non-linearity for wind loads.

For a transmission tower structure, the drag coefficient $C_D$ in Eq. (26) is described by the shape factor. Taking the effect of the wind yaw angle into account, the term $C_D A_s$ of the $i$-th tower section is given by Eq. (27) (IEC60826 2003, GB 50545-2012).

$$\begin{aligned} C_{Dt}^i A_s^i = &\left[1+0.2\sin^2(2\phi^*)\right] \\ &\cdot\left(\mu_{s,t}^i A_{s,t}^i \cos^2\phi^* + \mu_{s,l}^i A_{s,l}^i \sin^2\phi^*\right) \end{aligned} \tag{27}$$

where $i$ is the number index of tower sections; $\mu_z$ is a combined wind factor accounting for the altitude and terrain effects; $\varphi^*$=90°-$\varphi$ is the wind angle of attack to the transmission line; $A_{s,t}$ and $A_{s,l}$, $\mu_{s,t}$ and $\mu_{s,l}$ are the projected areas and shape factors of the transverse and longitudinal faces of the tower, respectively ('transverse' and 'longitudinal' express the directions that cross line and along line respectively). The term [1+ 0.2sin$^2$(2$\varphi^*$)] is an amplification factor with the maximum equal to 1.2 when $\varphi^*$ gets to 45°.

The resultant wind load acting on $i$-th tower section can be written as Eq. 28. $z_i$ represents the height of the $i$-th tower section; $x_i$ represents the horizontal coordinate of the $i$-th tower section; $\dot{X}^i(t)$ means the velocity response of $i$-th tower section at the time of $t$.

$$\begin{aligned} F_T^i(t) = &0.625\cdot\left[\bar{U}\left(z_i,t\right)+u\left(z_i,x_i,t\right)-\dot{X}^i(t)\right]^2\cdot \\ &\cdot\left[1+0.2\sin^2(2\phi^*)\right] \\ &\cdot\left(\mu_{s,t}^i A_{s,t}^i \cos^2\phi^* + \mu_{s,l}^i A_{s,l}^i \sin^2\phi^*\right) \end{aligned} \tag{28}$$

The resultant wind load is usually decomposed into two components that transverse and longitudinal to the line (Eqs. (29) and (30)).

$$F_{T,t}^i(t) = F_T^i(t)\times\cos\phi^* \tag{29}$$

$$F_{T,l}^i(t) = F_T^i(t)\times\sin\phi^* \tag{30}$$

Similarly, the wind load on the $j$-th point of transmission wires is expressed as Eq. (31) (GB 50545-2010, DL/T 5551-2018).

$$\begin{aligned} F_L^j(t) = &0.625\cdot\left[\bar{U}\left(z_j,t\right)+u\left(z_j,x_j,t\right)-\dot{X}^j(t)\right]^2 \\ &\cdot\sin^2\phi\cdot\mu_{s,w}^j\cdot d_j\cdot l_j \end{aligned} \tag{31}$$

where $j$ denotes the spatial point on transmission wires; $z_j$ and $x_j$ means the height and horizontal coordinate of the $j$-th point; $\dot{X}^j(t)$ is the velocity response of the $j$-th point at the time of $t$. $\mu_{s,w}$ is the shape factor of transmission wires. $d$ is the outer-diameter of wires and $l$ means the length of the wire section that corresponds to the point $j$. Here, just the wind effect that transverse to the line is considered (i.e., the load direction is transverse to the line) and therefore the term sin$^2\varphi$ is adopted to amend the wind-loading area of each wire section. For the example two-span TL system, geometrical parameters (e.g., projected areas, outer diameters of wires) and interaction parameters (e.g., shape factor) involved in the wind load calculation are determined depending on the design codes (GB 50545-2010, DL/T 5551-2018, GB 50009-2019).

The dynamic equation of structures subjected to winds is given by

$$M\ddot{X}_{t+\Delta t} + C\dot{X}_{t+\Delta t} + F_{t+\Delta t}^r = F_{t+\Delta t}^w \tag{32}$$

Where

$$F_{t+\Delta t}^w = \frac{1}{2}\rho_{air}\left(\bar{U}+u-\dot{X}_t\right)^2\cdot C_D A_s \tag{33}$$

$M$ and $C$ represent the mass matrix and damping matrix of the structure, respectively. $F_{t+\Delta t}^r$ and $F_{t+\Delta t}^w$ are the restoring force of the structure and the wind load at the time of $t$+$\Delta t$ ($\Delta t$ is the time increment of loading), respectively. Then, the wind load at time $t$+$\Delta t$ is influenced by the structural velocity response at time $t$, which results in the nonlinearity of the wind load. Typically, the quadratic drag term introduced by $u$ and $\dot{X}$ shown in Eq. (26) and Eq. (33) is ignored. Some studies show that the influence of the quadratic term on the mean-square response of structures is negligible when the wind fluctuation intensity is moderate, while the importance of the quadratic term to structural response extremes is much greater (Kareem and Tognarelli 1998). In this study, we intend to consider the influence of the nonlinear term on wind loads and structural responses, as the typhoon impact is concerned and the conductors connected to towers are characterized by the geometric-nonlinearity significantly. Then, in the simulation, the velocity response of structures is traced and used to calculate/update the wind load at the next increment step.

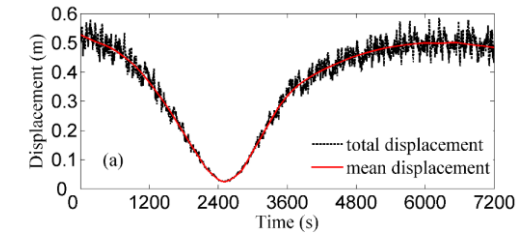


(a) total value and mean value

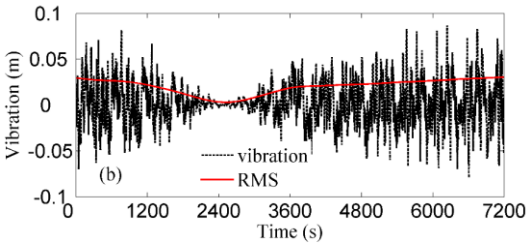


(b) vibration value and its RMS

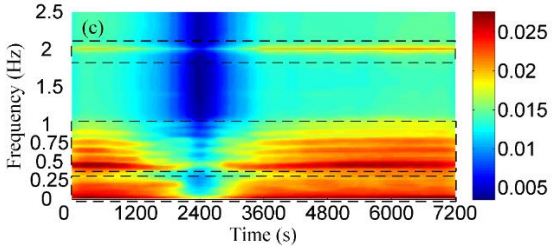


(c) EPSD of the vibration component

Fig. 11 Displacement at the top of tower structure

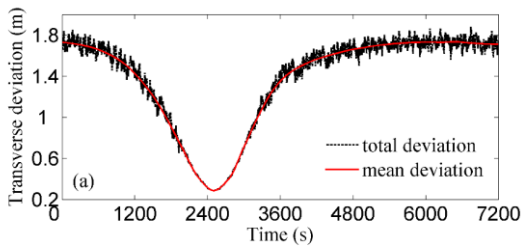


(a) total value and mean value

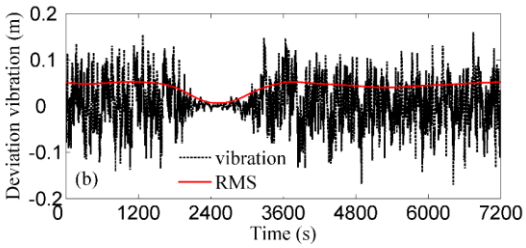


(b) vibration value and its RMS

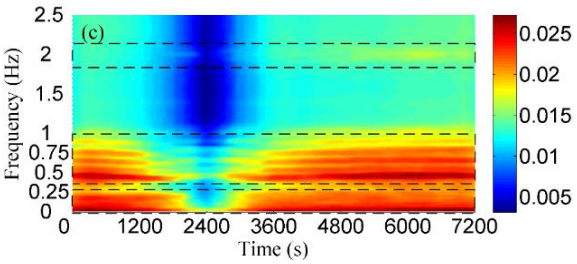


(c) EPSD of the vibration component

Fig. 12 Transverse deviation of the middle insulator

## 4. Simulation results

The example two-span TL system is simulated by a finite element model with tower members modeled by the beam element and transmission wires modeled by numerous consecutive truss elements. According to the structural design information and the load codes of overhead transmission line (GB 50545-2010, DL/T 5551-2018), projected areas and shape factors of each tower section (cross arms are contained) are listed in Table A1 in the appendix A, and first vibration mode of the tower structure are involved in Table A1. The damping ratio of the tower structure is taken to be 0.01 and the material damping with the coefficient of 0.001 is considered for the transmission wires. According to the diameters of transmission wires shown in Table 2, the shape factors $\mu_{s,w}$ of the conductor and ground wire are taken to be 1.0 and 1.1 respectively. The typhoon-induced dynamic simulation is done to the TL model, considering the time period of 14:00~16:00 of the typhoon event shown in Fig. 3. The typhoon-induced dynamic loads and structural responses are concerned in the following analysis.

### *4.1 Typhoon-induced responses of TL System*

The displacement at tower top which reflects the overall deformation of the tower structure, the wind-induced yaw of insulators which suggests the transverse deviation of conductors and the dynamic stress of insulators which indicates the wind-induced force that transferred from conductors to the tower are of concern in the following.

Fig. 11(a) first gives the generated time history of the total displacement at tower top with its time-varying mean value averaged by 10 min. The vibration component is extracted and shown as Fig. 11(b), and the corresponding EPSD is figured out with the sampling frequency taken to be 5 Hz.

According to Figs. 11(a) and 11(b), the time-varying mean displacement and the time-varying root mean square (RMS) of the vibrating displacement demonstrate the non-stationarity of the displacement response. From the EPSD of vibration (Fig. 11(c)), it shows three dominant frequency bands, i.e., 0~0.25 Hz, 0.5~1.0 Hz and near 2 Hz, which correspond to the wind fluctuation, the wind-induced vibration of conductors and the natural vibration of tower structure, respectively. The vibration properties of conductors are significantly influenced by their longitudinal tensions. From Fig. 11(c), the excited vibrations of conductors range from 0.5 Hz to 1.0 Hz. The first vibration frequency of transmission tower is around 2 Hz (see Table 2). The three-band-highlighted EPSD suggests the interaction between the wind and tower structure, as well as, the coupling effect of the TL system (i.e., the reaction of transmission wires to the tower structure).

The wind-induced yaw of insulators is defined by the transverse relative deviation between two end points of insulators. Then, taking the middle conductor and insulator as the example, Fig. 12 shows the wind-induced deviation in time and frequency domains. Further, considering the

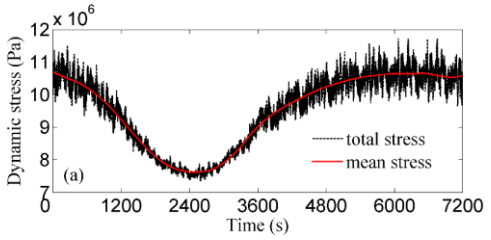


(a) total value and mean value

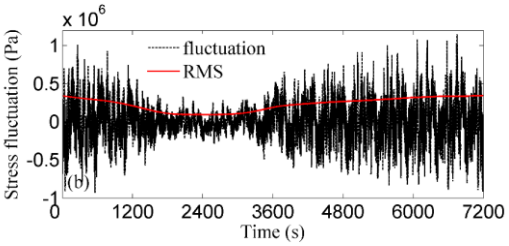


(b) vibration value and its RMS

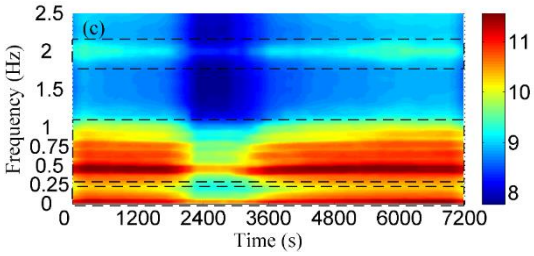


(c) EPSD of the vibration component

Fig. 13 Dynamic stress of the middle insulator

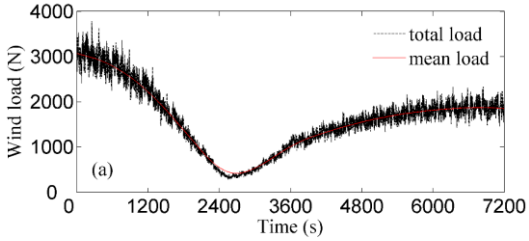


(a) time history

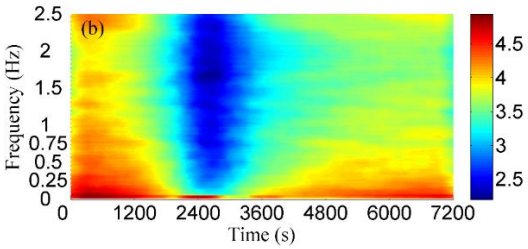


(b) EPSD

Fig. 14 Resultant wind load on tower section NO. 7

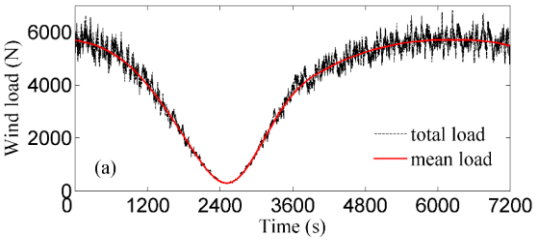


(a) time history

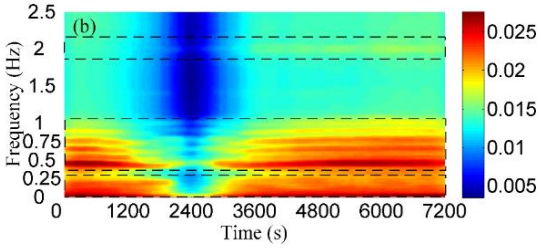


(b) EPSD

Fig. 15 Resultant wind load transferred from the middle conductor to the tower structure

dynamic stress of insulator, Fig. 13 gives the time history and EPSD of the wind-induced stress that transferred from conductors to the tower.

Similar to the displacement response at tower top, both of the wind-induced yaw and transferred dynamic stress are characterized by the non-stationarity with their mean values and RMSs varying with time. Three conspicuous frequency ranges are observed as well, by which the effect of wind fluctuation, and resulting vibrations of conductors and towers are uncovered.

### *4.2 Typhoon-induced dynamic loads*

According to the wind loading rule, the resultant wind load at each time increment step is calculated with the structural velocity response considered (see Eq. (33)), based on which Fig. 14(a) first gives the simulated time history of the wind load acting directly on the tower sections NO. 7 (see Fig. 9), and then generates the time history of the mean wind load with the averaging time of 10 min. Fig. 14(b) further shows the corresponding EPSD of fluctuating load with the sampling frequency taken to be 5 Hz.

From Eq. (28), the time history of wind load is jointly influenced by the time-varying wind speed and the time-varying wind angle of attack. In Fig. 14, we see similarly to the wind speed, the fluctuation of the wind load intensifies/weakens along with the increasing/decreasing of its mean value.

Concerning the connecting component between the tower structure and conductors (i.e., insulators), Fig. 15 gives the time history and EPSD of the wind load that transferred from the middle conductor to the tower structure using the simulated dynamic stress response and the cross-section size of insulator.

According to Eq. (31), the wind yaw angle significantly influences the wind load acting on wires. Hence, the increasing tendency of the mean value in Fig. 15 is greater than that of the wind speed (see Fig. 5) when the wind yaw angle keeps in a high level (i.e., $t > 3600$s, see Fig. 10). Fig 15(b) shows remarkable fluctuating components in the range of 0.5 Hz to 1.0 Hz, which demonstrates the effect of conductor vibration on the wind load. This effect is involved in the load calculation by considering the relative speed between the wind and structural velocity response (Eq. (26)). It is noteworthy, comparatively, the effect of tower vibration on the wind load acting on tower sections is less obvious (see Fig. 14(b)). In Fig 15(b), the near-2 Hz

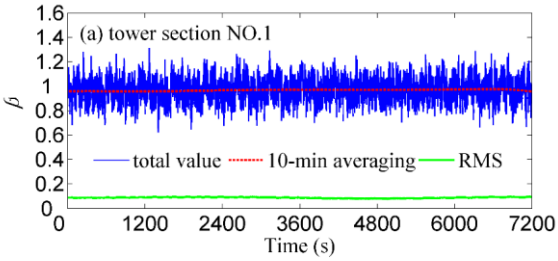


(a) tower section NO.1

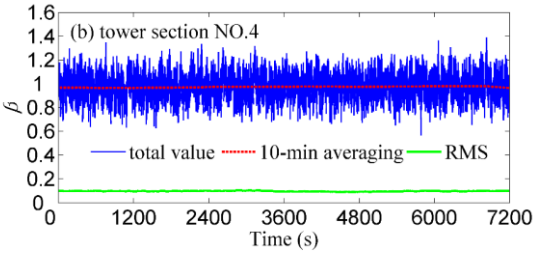


(b) tower section NO.4

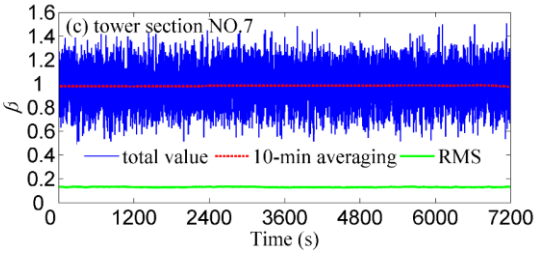


(c) tower section NO.7

Fig. 16 Time histories of the dynamic equivalent factor of tower $\beta$

frequency component can be carefully observed, which offers a glimpse of the coupling effect between the tower and wires from the perspective of loads.

## 5. Discussions

According to Eq. (28), the time-varying feature of wind load on the $i$-th tower section is determined by the quadratic term $\left[\bar{U}(z_i,t)+u(z_i,x_i,t)-\dot{X}^i(t)\right]^2$. Here, use $G$ to denote this term and take the 10m over ground as the reference height, then $G$ can be expanded as Eq. (34).

$$\begin{aligned} G &= \left[\bar{U}\left(z_i,t\right)\right]^2 + 2\bar{U}\left(z_i,t\right)\left[u\left(z_i,x_i,t\right)-\dot{X}^i(t)\right] \\ &\quad + \left[u\left(z_i,x_i,t\right)-\dot{X}^i(t)\right]^2 \\ &= \left[\frac{\ln\left(z_i/z_0\right)}{\ln\left(10/z_0\right)}\cdot U(10)\cdot f(t)\right]^2 + 2\frac{\ln\left(z_i/z_0\right)}{\ln\left(10/z_0\right)} \\ &\quad \cdot U(10)\cdot f(t)\cdot\left[u\left(z_i,x_i,t\right)-\dot{X}^i(t)\right] \\ &= \left[U(t)\right]^2\cdot\left[\mu(z_i)\right]^2\cdot\beta(z_i,x_i,t) \end{aligned} \tag{34}$$

Where

$$U(t)=U(10)\cdot f(t) \tag{35}$$

$$\mu(z_i)=\frac{\ln\left(z_i/z_0\right)}{\ln\left(10/z_0\right)} \tag{36}$$

$$\beta(z_i,x_i,t)=1+\frac{2\left[u\left(z_i,x_i,t\right)-\dot{X}^i(t)\right]}{\mu(z_i)\cdot U(t)} \tag{37}$$

In Eq. (34), the term $G$ is finally expressed by three parameter, i.e. $U(t)$, $\mu(z)$ and $\beta(z,x,t)$. $U(10)$ in Eq. (35) represents the mean wind speed at 10m over the ground and $f(t)$ is the corresponding time profile. Then, $U(t)$ is the time-varying mean wind speed at the reference height. The parameter $\mu(z)$ in Eq. (36), used to describe the vertical profile of the mean wind speed, is named as the height factor here and expressed by the logarithm rule. The height factor is determined jointly by the height of interest and the terrain type ($z_0$ is roughness length of the ground). According to Eq. (37), the parameter $\beta(z,x,t)$ describes the combination effect of the wind fluctuation, structural vibration and mean wind on the wind load, and changes with the time as well as the spatial points of TL system. Here, we name $\beta(z,x,t)$ as the dynamic equivalent factor of tower and its value is always larger than one.

Based on the simulation results, the dynamic equivalent factor of each tower section and cross arms can be calculated. Fig. 16 shows the calculated dynamic equivalent factors of the tower sections NO. 1, 4, 7, with their mean values averaged by 10min and RMSs considered. Time histories in Fig. 16 demonstrate the stationary feature with mean values and RMSs keeping constant in the process, although the wind fluctuation and structural velocity response that involved in the calculation of factor $\beta$ are characterized by non-stationarities. Due to the quadratic drag term introduced by $u$ and $\dot{X}$ shown in Eq. (33) is considered in the simulation, the minus between the wind fluctuating $u$ and the structural velocity response $\dot{X}$ weakens the non-stationarity dramatically for the wind load.

Similar to the wind load acting on tower structure, the wind load on transmission conductors can also be addressed by the above way. Instead of the wind load calculated at each point of the conductor (Eq. (31)), here we pay more attention to the equivalent wind load that transferred from conductors to the tower. We concern the whole conductor and yield the transferred wind load according to the simulated dynamic stress in connecting components (i.e., insulators). Then, for the $k$-th conductor, the transferred wind load is written as Eq. 38 by adopting three parameters, $U(t)$, $\mu(z)$ and $\alpha(z,x,t)$.

$$\begin{aligned} H^k &= 0.625\cdot\left\{\left[U(t)\right]^2\cdot\left[\mu(z_k)\right]^2\cdot\alpha(z_k,x_k,t)\right\} \\ &\quad \cdot\sin^2\phi\cdot\mu_{s,w}^k\cdot L_h \end{aligned} \tag{38}$$

$L_h$ is the horizontal span of transmission line and equal to the average of two adjacent spans. Same as Eqs. (35) and 36, $U(t)$ and $\mu(z)$ in Eq. (38) have the identical explanations and expressions. Differing from $\beta$, the parameter $\alpha$ in Eq. (38) cannot be expressed analytically as it is an equivalent coefficient that refers to the overall along-span effect of the

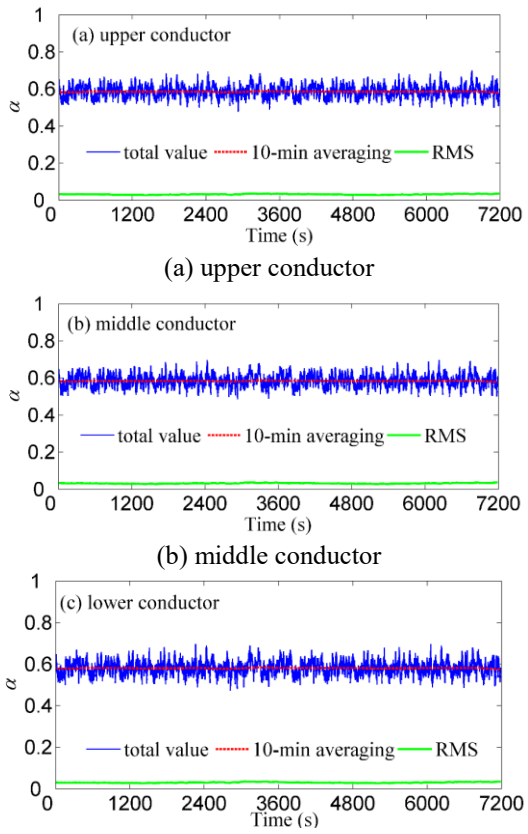


(a) upper conductor

(b) middle conductor

(c) lower conductor

Fig. 17. Times histories of the dynamic equivalent factor of conductor $\alpha$

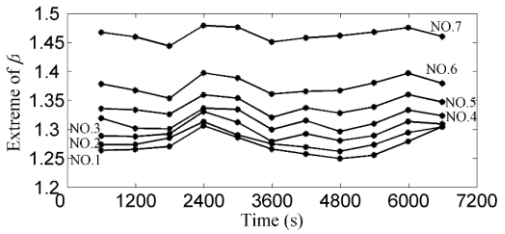


Fig. 18 Extreme estimation for $\beta$

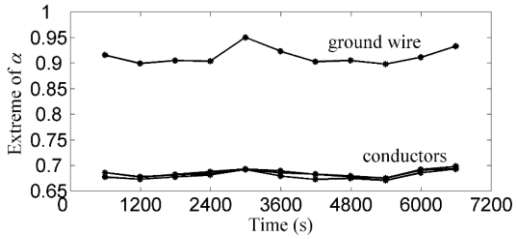


Fig. 19 Extreme estimation for $\alpha$

wind fluctuation and conductor vibration. Here, we name $\alpha$ as the dynamic equivalent factor of conductor and calculate it according to the dynamic stress of insulator. Fig. 17 shows the resultant $\alpha$ for each conductor.

Distinct from the wind fluctuation and structural responses, the dynamic equivalent factor of conductor $\alpha$ shows the stationary tendency in the process, according to the time histories of mean values and RMSs shown in Fig. 17. It is noteworthy, differing from the dynamic equivalent factor of tower $\beta$, the yielded factor $\alpha$ is no larger than 1. This is because the dynamic equivalent factor of conductor takes into account both of the dynamic amplification effect and the effect of non-uniformly along-line distribution of wind. Being less than one indicates the reduction effect of non-uniformly distribution of wind exceeds the dynamic amplification effect.

Given the fluctuating $\beta$ has the stationary Gaussian distribution, the peak factor method is adopted here to estimate the extreme value of $\beta$ (Eqs. (39) and (40)) with the standard sampling time interval taken to be 10 min, for each tower section.

$$\tilde{\beta} = \bar{\beta} + \nu \cdot \sigma_{\beta} \tag{39}$$

$$\nu = \sqrt{2 \cdot \ln N_{cross}} + 0.5772 \Big/ \sqrt{\ln N_{cross}} \tag{40}$$

$\tilde{\beta}$ denotes the estimated extreme value; $\bar{\beta}$ is the 10-min mean value of $\beta$ and $\sigma_{\beta}$ represents the corresponding RMS; $\nu$ denotes the peak factor calculated by Eq. 40; $N_{cross}$ is the number of times of crossing the mean value $\bar{\beta}$. By estimation, Fig. 18 yields the extremes of dynamic equivalent factor of each tower section. Extremes of the dynamic equivalent factor $\alpha$ are estimated as well using the same approach and Fig. 19 shows the extremes of $\alpha$ for each conductor.

For the structural design (just the stationary normal wind is concerned), the wind load acting on tower sections is usually addressed as the static load, in which the gust response factor is adopted to consider the dynamic amplification effect on the structural responses. The gust response factor (denoted by $\beta_z$) is treated as the ratio of the wind-induced inertial load to the average wind load, which is jointly influenced by the wind fluctuation and structural dynamic properties. According to the load codes (DL/T 5551-2018, GB 50009-2019), $\beta_z$ is calculated depending on the wind turbulence intensity, the resonant and background factors of structural responses. Based on the design information of the concerned transmission line, Table A1 in the appendix A further gives the transverse and longitudinal gust response factors of each tower section that are recommended by DL/T 5551-2018. The commonly used calculation method of the wind-induced inertial load depends on the stationary and linear assumptions, in which the wind fluctuation spectrum is stationary and the frequency-based transfer function is constructed based on the linear superposition. It is unreliable to apply the calculation method directly to the case of typhoon-induced behavior of transmission TL system. In this paper, we consider the dynamic effect of wind loads by introducing the quadratic drag term. The constructed dynamic equivalent factor of tower indicates the ratio of the total wind load to the mean wind load, which describes the combination effect of the wind fluctuation, structural vibration and mean wind on the wind load, and changes with the time as well as the spatial points of TL system. Though the extreme of dynamic equivalent factor is not

identical with the gust response factor, the two types of factors are jointly influenced by the wind fluctuation and structural dynamic properties. Therefore, we do the comparison of the two factors and get some results for reference. The comparison results show that the gust response factor of tower section NO.1 is less than its estimated extreme of dynamic equivalent factor, which indicates the tower design may not be safe with the typhoon impact involved.

As for the wind load that is transferred from conductors to the tower structure, two parameters are commonly adopted for the structural design, i.e., the gust factor (denoted by $\beta_C$) accounting for the effect of wind fluctuation and the span factor (denoted by $\alpha_L$) accounting for the effect of non-uniformly distribution of wind along the span. The gust factor and span factor suggested by DL/T 5551-2018 are calculated and shown in Table A2 of the appendix A. Comparing the estimated extremes of the dynamic equivalent factor of conductor $\alpha$ shown in Fig.19 (who jointly takes into account the wind fluctuation effect and the effect of non-uniformly distribution wind) with the suggested value of $\beta_C$*$\alpha_L$ (shown in Table A2), it is indicated that the two recommended design factors are satisfactory as well when the typhoon impact is concerned.

## 6. Conclusions

This paper offers fundamental insights on the simulation of typhoon wind, and typhoon-induced loads and responses of the electric transmission tower-line system. The surface mean wind induced by typhoon is first simulated with the radial profile, the vertical profile and the near-surface mean wind conversion rule clarified in detail, in which the spatiotemporal feature of typhoon events is considered in terms of the large scale. The non-stationary fluctuation of typhoon wind is addressed with a modulation function and then generated using the modified spectral representation method with the correlation in the longitudinal-vertical plane considered, in which the time-varying feature of typhoon wind field is concerned in terms of the small scale.

Combining the typhoon simulation with the finite element modeling of tower-line system, typhoon-induced wind field to TL system and dynamic simulations are carried out depending on the wind loading rule. Wind loads on the tower structure and transmission wires are calculated/updated with the change of wind speed, wind yaw angle and structural responses.

Vibrations of the tower and conductors show the feature of non-stationarity with the time-varying mean components and RMSs. Fluctuating responses are addressed both in the time and frequency domains using the evolutionary power spectral density (EPSD) function, by which the coupling effect between the tower and wires is uncovered. EPSDs of typhoon-induced dynamic loads (i.e., wind loads acting on the tower structure and transferred from conductors to the tower) show that, compared with the tower, the vibration of conductors makes more obvious effects on the wind loading.

The resultant wind loads acting on the tower and transferred from conductors are treated by the constructed dynamic equivalent factor $\beta$ and dynamic equivalent factor $\alpha$, respectively. Differing from the wind fluctuation and structural responses, the simulated $\beta$ and $\alpha$ are characterized by the stationarity with their mean values and RMSs keeping in steady during the typhoon event. The simulated wind load is determined by the square of the difference between the wind and the structural vibrating velocity, which results in the non-stationarity fading out for the dynamic loads. Then, it is concluded that the non-stationary fluctuating wind contributes to the stationary dynamic loads and non-stationary responses of TL system.

The comparison between the estimated extremes of $\beta$ and the gust response factor recommended by design codes, indicates that the suggested gust response factor for the lower section of tower may not be safe when the typhoon impact is involved. Comparing the estimated extremes of $\alpha$ with the suggested design parameters (including the gust factor and the span factor), it demonstrates the recommended gust factor and span factor for wires are safe enough even under the typhoon cases.

## Acknowledgments

The financial support from National Natural Science Foundation of China under Grant no. 51278369 is gratefully acknowledged.

## References

Battista, R.C., Rodrigues, R.S. and Pfeil, M.S. (2003), "Dynamic behavior and stability of transmission line towers under wind forces", *J Wind Eng Ind Aerodyn*, **91**(8), 1051-1067. https://doi.org/10.1016/S0167-6105(03)00052-7.

Cai, Y.Z. and Wan, J.W. (2021), "Wind-resistant capacity modeling for electric transmission line towers using kriging surrogates and its application to structural fragility", *Appl. Sci-Basel*, **11**(11), 4714. https://doi.org/10.3390/app11114714.

Cai, Y.Z., Xie, Q., Xue, S.T., Hu, L. and Kareem, A. (2019), "Fragility modelling framework for transmission line towers under winds", *Eng Struct*, **191**, 686-697. https://doi.org/10.1016/j.engstruct.2019.04.096.

Charnock H (1955), "Wind stress on a water surface", *Q J R Meteorolog Soc*, **81**(350): 639-640.

Chavas, D.R. and Lin, N. (2016), "A model for the complete radial structure of the tropical cyclone wind field part II: Wind field variability", *Amer. Meteor. Soc.*, **73**, 3093-3113. https://doi.org/10.1175/JAS-D-15-0185.1.

Chavas, D.R., Lin, N. and Emanuel, K. (2015), "A model for the complete radial structure of the tropical cyclone wind field part I: Comparison with observed structure", *Amer. Meteor. Soc.*, **72**, 3647-3661. https://doi.org/10.1175/JAS-D-15-0014.1.

Chen, Y. and Duan, Z.D. (2018), "A statistical dynamics track model of tropical cyclones for assessing typhoon wind hazard in the coast of southeast China", *J Wind Eng. Ind. Aerod.*, **172**, 325-340. https://doi.org/10.1016/j.jweia.2017.11.014.

DL/T 5551-2018 (2018), *Load Code for the Design of Overhead Transmission Line*, Electric Power Planning & Engineering Institute, Beijing, China.

Donelan, M., Haus, B., Reul, N., Plant, W., Stiassnie, M., Graber, H., Brown, O. and Saltzman, E. (2004), "On the limiting aerodynamic roughness of the ocean in very strong winds",

*Geophys. Res. Lett.*, **31**, L18306. https://doi.org/10.1029/2004GL019460.
Emanuel, K.A. (2011), "Self-stratification of tropical cyclone outflow part II: Implications for storm intensification", *J. Atmoss Sci.*, **69**, 988-996. https://doi.org/10.1175/JAS-D-11-0177.1.
Emanuel, K.A. and Rotunno, R. (2011), "Self-stratification of tropical cyclone outflow Part I: Implications for storm structure", *J. Atmos. Sci.*, **68**, 2236-2249. https://doi.org/10.1175/JAS-D-10-05024.1.
GB 50009-2019 (2019), *Load Code for the Design of Building Structures (National Standard)*, Ministry of Construction of the People's Republic of China, Beijing, China.
GB 50545-2010 (2010), *Code for Design of 110kV~750kV Overhead Transmission Line (National Standard)*, China Electricity Council, Beijing, China.
Holland, G.J., Belanger, J.I. and Fritz, A. (2011), "A revised model for radial profiles of hurricane winds", *Mon. Weather Rev.*, **138**, 4393-4401. https://doi.org/10.1175/2010MWR3317.1.
Huang, G.Q., Zheng, H.T., Xu, Y.L. and Li, Y.L. (2015), "Spectrum models for nonstationary extreme winds", *J. Struct. Eng.*, **141**(10), 04015010. https://doi.org/10.1061/(ASCE)ST.1943-541X.0001257.
Huang, M.F., Lou, W., Yang, L., Sun, B., Shen, G. and Tse, K.T. (2012), "Experimental and computational simulation for wind effects on the Zhoushan transmission towers", *Struct. Infrastruct. Eng.*, **8**(8), 781-799. https://doi.org/10.1080/15732479.2010.497540.
IEC 60826 (2003), *Design Criteria of Overhead Transmission Lines*, International Electro-technical Commission, Geneva, Switzerland.
IPCC (2013), Climate Change 2013: The Physical Science Basis, Contribution of Working Group I to the 5th Assessment Report of the Intergovernmental Panel on Climate Change.
Kareem, A. (2008), "Numerical simulation of wind effects: A probabilistic perspective", *J. Wind Eng. Ind. Aerod.*, **96**(10-11), 1472-1497. https://doi.org/10.1016/j.jweia.2008.02.048.
Kareem, A., Tognarelli, M.A. and Gurley, K.R. (1998), "Modeling and analysis of quadratic term in the wind effects on structures", *J. Wind Eng. Ind. Aerod.*, **74-76**, 1101-1110. https://doi.org/10.1016/S0167-6105(98)00101-9.
Li, L.X., Kareem, A., Xiao, Y.Q., Song, L.L. and Zhou, C.Y. (2015), "A comparative study of field measurements of the turbulence characteristics of typhoon and hurricane winds", *J. Wind Eng. Ind. Aerod.*, **140**, 49-66. https://doi.org/10.1016/j.jweia.2014.12.008.
Liang, S., Zou, L., Wang, D. and Cao, H. (2015), "Investigation on wind tunnel tests of a full aeroelastic model of electrical transmission tower-line system", *Eng. Struct.*, **85**, 63-72. https://doi.org/10.1016/j.engstruct.2014.11.042.
Lin. N. and Chavas, D. (2012), "On hurricane parametric wind and applications in storm surge modeling", *J. Geophys. Res.*, **117**, D09120. https://doi.org/10.1029/2011JD017126.
Meng, Y., Matsui, M. and Hibi, K. (1997), "A Numerical study of the wind field in a typhoon boundary layer", *J. Wind Eng. Ind. Aerod.*, **67-68**, 437-448. https://doi.org/10.1016/S0167-6105(97)00092-5.
Paluch, M.J., Cappellari, T.T.O. and Riera, J.D. (2007), "Experimental and numerical assessment of EPS wind action on long span transmission line conductors", *J. Wind Eng. Ind. Aerod.*, **95**(7), 473-492. https://doi.org/10.1016/j.jweia.2006.09.003.
Phadke, A.C., Martino, C.D., Cheung, K.F. and Houston, S.H. (2003), "Modeling of tropical cyclone winds and waves for emergency management", *Ocean Eng*, **30**(4), 553-578. https://doi.org/10.1016/S0029-8018(02)00033-1.
Riehl, H. (1954), *Tropical Meteorology*, McGraw-Hill.
Schloemer, R.W. (1954), *Analysis and Synthesis of Hurricane Wind Patterns Over Lake Okeechobee, Florida*, Hydrometeorological Rep. 31, Department of Commerce and U.S. Army Corps of Engineers, U.S. Weather Bureau, Washington, DC.
Shinozuka, M. and Deodatis, G. (1991), "Simulation of stochastic processes by spectral representation", *Appl. Mech. Rev.*, **44**(4), 191-204. https://doi.org/10.1115/1.3119501.
Simiu, E. and Scanlan, R.H. (1996), *Wind Effects on Structures* New York: Wiley.
Takeuchi, M., Maeda, J. and Ishida, N. (2010), "Aerodynamic damping properties of two transmission towers estimated by combining several identification methods", *J. Wind Eng. Ind. Aerod.*, **98**(12), 872-880. https://doi.org/10.1016/j.jweia.2010.09.001.
Tao, T.Y., Shi, P. and Wang, H. (2020), "Spectral modelling of typhoon winds considering nexus between longitudinal and lateral components", *Renew. Energy* **162**, 2019-2030. https://doi.org/10.1016/j.renene.2020.09.130.
Tao, T.Y. and Wang, H. (2019), "Modelling of longitudinal evolutionary power spectral density of typhoon winds considering high-frequency subrange", *J. Wind Eng. Ind. Aerod.*, **193**, 103957. https://doi.org/10.1016/j.jweia.2019.103957.
Vaiman, M., Bell, K., Chen, Y., Chowdhury, B., Dobson, I., Hines, P. and Zhang, P. (2012), "Risk assessment of cascading outages: methodologies and challenges", *IEEE Trans. Power Syst*, **27**(2), 631-41. https://doi.org/10.1109/TPWRS.2011.2177868.
Vickery, P.J., Wadhera, D., Powell, M.D. and Chen, Y. (2009), "A hurricane boundary layer and wind field model for use in engineering applications", *J. Appl. Meteorol. Climatol*, **48**, 381-404. https://doi.org/10.1175/2008JAMC1841.1.
Wang, D.H., Chen, X.Z. and Xu, K. (2017), "Analysis of buffeting response of hinged overhead transmission conductor to nonstationary winds", *Eng. Struct*, **147**, 567-582. https://doi.org/10.1016/j.engstruct.2017.06.009.
Xiao, Y.F., Duan, Z.D., Xiao, Y.Q., Ou, J.P., Chang, L. and Li, Q. S. (2011), "Typhoon wind hazard analysis for southeast China Coastal Regions", *Struct. Saf.*, **33**(4-5), 286-295. https://doi.org/10.1016/j.strusafe.2011.04.003.
Xie, Q., Cai, Y.Z. and Xue, S.T. (2017), "Wind-induced vibration of UHV transmission tower line system: wind tunnel test on aero-elastic model", *J. Wind Eng. Ind. Aerod.*, **171**, 219-29. https://doi.org/10.1016/j.jweia.2017.10.011.

*AD*

## Appendix A: Parameters used for the simulation and structural design

Table A1 Structural, load and design parameters of the tower structure

| Total Height (m) | | Wind pressure (kPa) | | Design wind speed (10 m over the ground, m/s) | | | | Frequency (Hz) | | Gust response factor $\beta_z$ | |
|---|---|---|---|---|---|---|---|---|---|---|---|
| 45.5 | | 0.70 | | 33.5 | | | | transverse | longitudinal | | |
| | | | | transverse | | longitudinal | | 2.037 | 2.047 | transverse | longitudinal |
| Tower sections $z$ (m) | | $\mu_z$ | $I_z$ | $A_{s,t}$ (m$^2$) | $\mu_{s,t}$ | $A_{s,l}$ (m$^2$) | $\mu_{s,l}$ | $\delta$ | $m$ (kg) | $\beta_{z,t}$ | $\beta_{z,l}$ |
| NO. 1 | 6.4 | 1.0000 | 1.069 | 4.5330 | 0.3005 | 4.5330 | 0.3005 | 0.013 | 1958.4 | 1.131 | 1.130 |
| NO. 2 | 12.8 | 1.0769 | 0.964 | 4.2195 | 0.3334 | 4.2195 | 0.3334 | 0.057 | 1399.7 | 1.452 | 1.451 |
| NO. 3 | 19.2 | 1.2162 | 0.907 | 3.7107 | 0.3561 | 3.7107 | 0.3561 | 0.132 | 1280.1 | 1.762 | 1.761 |
| NO. 4 | 25.6 | 1.3258 | 0.868 | 3.3701 | 0.4091 | 3.3701 | 0.4091 | 0.248 | 1030.4 | 2.021 | 2.020 |
| NO. 5 | 33 | 1.4307 | 0.836 | 4.0502 | 0.4573 | 4.7056 | 0.5130 | 0.453 | 1508.7 | 2.035 | 2.190 |
| NO. 6 | 39 | 1.5042 | 0.815 | 2.8436 | 0.5272 | 3.5406 | 0.5666 | 0.692 | 1120.7 | 2.056 | 2.233 |
| NO. 7 | 45.5 | 1.5754 | 0.797 | 3.1369 | 0.5961 | 3.8577 | 0.4847 | 1.000 | 1165.4 | 2.075 | 2.318 |

* $I_z$ is the suggested wind turbulence intensity at the height of $z$; $\delta$ is the first vibration mode of the tower structure; $m$ is the mass of each tower section; $\beta_{z,t}$ and $\beta_{z,l}$ are the gust response factors of tower sections along the transverse and longitudinal directions, respectively.

Table A2 Structural, load and design parameters of transmission wires (ground wires and conductors are included)

| Horizontal span (m) | Fluctuation intensity (10 m over the ground, $I_{10}$) | Roughness coefficient | Peak factor | Wind-fluctuation-based reduction factor | Span-based integral factor | Wind-load-based reduction factor |
|---|---|---|---|---|---|---|
| 271.5 | 0.14 | 0.15 | 2.5 | 0.7 | 0.4769 | 0.9 |
| Wires | $z$ (average altitude, m) | $\mu_z$ | $I_z$ | $\beta_C$ | $\alpha_L$ | $\beta_C$*$\alpha_L$ |
| ground wire | 45.50 | 1.5754 | 0.1115 | 1.402 | 0.761 | 1.068 |
| up conductor | 39.76 | 1.5130 | 0.1138 | 1.412 | 0.758 | 1.071 |
| middle conductor | 33.76 | 1.4405 | 0.1166 | 1.425 | 0.754 | 1.075 |
| down conductor | 27.76 | 1.3584 | 0.1201 | 1.441 | 0.750 | 1.080 |

* $I_z$ is the suggested wind turbulence intensity at the height of $z$; $\beta_C$ is gust factor of wind; $\alpha_L$ is the span factor.